Computers and Geotechnics 177 (2025) 106897

Contents lists available at ScienceDirect

Computers and Geotechnics

journal homepage: www.elsevier.com/locate/compgeo

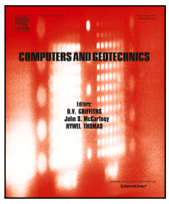

Research paper

Nonlinear Mohr–Coulomb yield criterion: Integration in ADMM-based finite element limit analysis formulation and application to slope stability assessment

M. Vicente da Silva

Department of Civil Engineering, School of Science and Technology, NOVA University Lisbon, Campus da Caparica, 2829-516 Caparica, Portugal

ARTICLE INFO

Keywords:
Nonlinear Mohr–Coulomb
Limit analysis
Lower bound
Upper bound
Alternating direction method of multipliers (ADMM)
Slope stability

ABSTRACT

This paper details the implementation of a nonlinear yield criterion in an ADMM-based finite element limit analysis formulation. The criterion represents a generalization of the widely used Mohr–Coulomb criterion. The current formulation is designed to provide rigorous upper and lower bound solutions for plane strain condition problems.

The effectiveness of this new numerical tool is demonstrated through its application to the traditional geotechnical problem of slope stability analysis. Highly accurate slope stability factors are determined for a practical range of soil parameters, and the results are validated against values proposed by other authors whenever such data is available.

1. Introduction

The linear Mohr–Coulomb failure criterion remains widely used in geotechnical engineering, although there is consistent experimental evidence demonstrating nonlinear variations in soil shear strength with changes in confining pressure, particularly noticeable at lower levels (Bishop et al., 1965; Ponce and Bell, 1971; Fukushima and Tatsuoka, 1984; Maksimovic, 1989; Perry, 1994; Lancelot et al., 2006; Chakraborty and Salgado, 2010).

Research into numerical limit analysis using a nonlinear Mohr–Coulomb-based yield criterion appears to have emerged in the 1980s (Baker and Frydman, 1983; Zhang and Chen, 1987; Drescher and Christopoulos, 1988), representing a notable effort to address this observed nonlinearity. These studies were based on the upper-bound method and rooted in the optimization of semi-analytical failure mechanisms. Despite its effectiveness, this method is constrained by the necessity to tailor failure mechanisms for each unique problem and is not adaptable for producing lower-bound solutions. Notwithstanding these limitations, when dealing with a nonlinear Mohr–Coulomb criterion, the semi-analytical technique continues to be utilized in recent works for obtaining upper-bound solutions (Yang and Yin, 2004; Yang and Long, 2015; Yu et al., 2019; Wu et al., 2019). Also following the upper-bound approach, Zhang and Smith (2020) presents an alternative technique based on multi-wedge rigid-block mechanisms. They also propose coupling their method with the Discontinuity Layout Optimization (DLO) method (Smith and Gilbert, 2007). This strategy eliminates the need for pre-established mechanisms and can be applied to a wide range of problems, offering a more flexible and comprehensive solution scheme.

Although the early works laid the groundwork, the Finite Element Limit Analysis (FELA) field did not widely embrace this path. As far as we know, existing formulations that employ this kind of nonlinear yield criterion are extremely limited. One notable exception is a lower-bound finite element limit analysis formulation described by Li and Cheng (2012).

We attribute this predominant reliance to the challenging task of effectively incorporating the constraints imposed by nonlinear yield conditions within mathematical programming algorithms. To overcome this issue, Li and Cheng (2012) introduced an approximation of the yield function, resulting in a formulation that does not qualify as a strict lower-bound approach. Recently, Korada and Kumar (2023) proposed a novel formulation that offers a fresh perspective on managing the nonlinear yield condition within the framework of Finite Element Limit Analysis (FELA). The authors base their formulation on interior-point optimization, a widely adopted method in many state-of-the-art FELA formulations (Pastor et al., 2003; Makrodimopoulos and Martin, 2005; Martin, 2005; Krabbenhøft et al., 2007, 2008; Pastor et al., 2008). As a key innovation, they introduce the yield condition using power cone constraints. Power cone programming (PCP) is an extension of second-order cone programming (SOCP) (Nesterov, 2012) and has previously been applied in the context of FELA to model the Hoek–Brown strength criterion (Kumar and Rahaman, 2020; Rahaman and Kumar, 2020).

E-mail address: vicente.silva@fct.unl.pt.

https://doi.org/10.1016/j.compgeo.2024.106897
Received 23 August 2024; Received in revised form 21 October 2024; Accepted 2 November 2024
Available online 18 November 2024

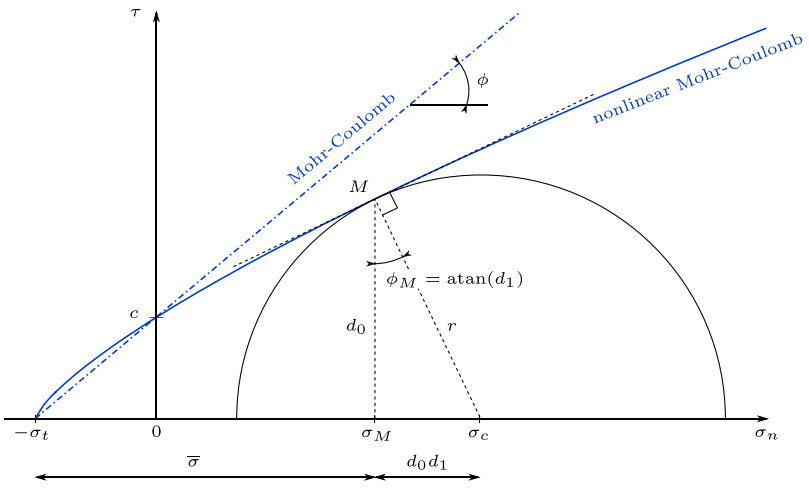

Fig. 1. Yield envelope of the NLMC criterion.

However, since the nonlinear Mohr–Coulomb criterion cannot be precisely represented by these conic constraints, Korada and Kumar (2023) developed a sequential PCP strategy for the lower-bound formulation. This consists of an iterative approach, where PCP steps are executed in each iteration. The downside of this iterative approach is the increased computational time and the lack of guaranteed attainment of strict lower bounds.

Additionally, the authors propose a complementary non-iterative strict upper-bound formulation that is also based on PCP. However, this formulation requires parameters, referred to as equivalent material cohesions and friction angles, that are derived from the lower-bound analysis, thereby creating a dependency between the two formulations.

The current research focuses on contributing to the existing need for formulations in this particular domain, with the specific objective of developing strict lower-bound and strict upper-bound formulations.

The author's research group has been developing numerical tools within the finite element framework for plastic limit analysis, employing the Alternating Direction Method of Multipliers (ADMM) (Boyd et al., 2011) as the solution scheme. The outcome of this effort (Vicente da Silva et al., 2020) is a finite element limit analysis (FELA) formulation that, among other attributes, demonstrates remarkable flexibility in efficiently handling a wide range of yield conditions. Recent works have precisely explored this capability by incorporating failure criteria that other FELA formulations struggle with, such as the Matsuoka–Nakai criterion (Vicente da Silva and Antão, 2023), the Lade–Duncan criterion (Antão and Vicente da Silva, 2022), the Hoek–Brown criterion (Vicente da Silva and Antão, 2024), and Bishop's anisotropic criterion (Vicente da Silva and Antão, 2025).

To implement the nonlinear Mohr–Coulomb criterion while ensuring the formulation can produce strict bounds and maintain efficiency, it is necessary to tailor a core part of the solution scheme. This paper provides a detailed description of the design of this crucial section of the formulation.

Following the development of the numerical tool, its effectiveness will be illustrated by examining the influence of the nonlinear criterion on slope stability analysis. Stability factors will be determined to demonstrate the practical benefits of the formulation.

2. Nonlinear yield criterion

In this work, we adopt a yield criterion that represents a nonlinear enhancement of the traditional Mohr–Coulomb (MC) criterion. This section aims not only to introduce and provide an overview of the criterion but also to present the mathematical framework necessary for its numerical implementation in our computational model. The yield envelope of this criterion, for the Mohr's circle representation, is expressed as:

$$\tau = c\left(1 + \frac{\sigma_n}{\sigma_t}\right)^a \tag{1}$$

Here, σ_n and τ represent the normal and shear stresses in Mohr's circle space, respectively. It is important to note that compression components are treated as positive throughout this paper. Cohesion is denoted by c, uniaxial tensile stress by σ_t, and a is a scalar parameter that can assume a value in the range $(0, 1]$.

This criterion is equivalent to that presented by Zhang and Chen (1987), with the difference that in their work, a nonlinear coefficient m is used, which is the inverse of a. When $a \ll 1$, the criterion approximates the Tresca criterion with a tension cut-off, a scenario not covered in this paper. When $a = 1$, it reverts to the classical Mohr–Coulomb (MC) criterion:

$$\tau = c + \tan(\phi)\sigma_n \tag{2}$$

where ϕ denotes the friction angle. In this case, the following equality holds:

$$\sigma_t = \frac{c}{\tan(\phi)} \tag{3}$$

The nonlinear Mohr–Coulomb (NLMC) failure envelope is illustrated in Fig. 1. Any stress state lying on the yield surface must be represented by a Mohr's circle tangent to the envelope. In the figure, the point of tangency is denoted as point M.

The Mohr's circle center, σ_c, and the radius, r, for a plastic stress state can be determined as follows:

$$\begin{cases} \sigma_c = \sigma_M + d_0 d_1 = -\sigma_t + \overline{\sigma} + d_0 d_1 \\ r = d_0 \eta \end{cases} \tag{4}$$

where,

$$\eta = \sqrt{1 + d_1^2} \tag{5}$$

In the above expressions, d_k represents the kth derivative of τ with respect to σ_n evaluated at point M. These derivatives are determined by the following formula:

$$d_k = \left.\frac{d^k \tau}{d\sigma_n^k}\right|_{\sigma_n = \sigma_M} = \frac{c}{\sigma_t}\left(1 + \frac{\sigma_M}{\sigma_t}\right)^{a-k} \prod_{i=0}^{k-1}(a - i) \tag{6}$$

Alternatively, by introducing the variable transformation,

$$\overline{\sigma} = \sigma_M + \sigma_t \tag{7}$$

the expression (6) becomes:

$$d_k = \frac{c}{\sigma_t}\left(\frac{\overline{\sigma}}{\sigma_t}\right)^{a-k} \prod_{i=0}^{k-1}(a - i) \tag{8}$$

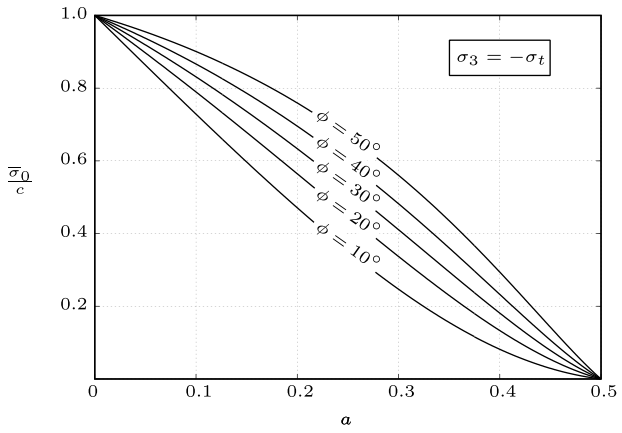

Fig. 2. Minimum threshold curves for $\overline{\sigma}$.

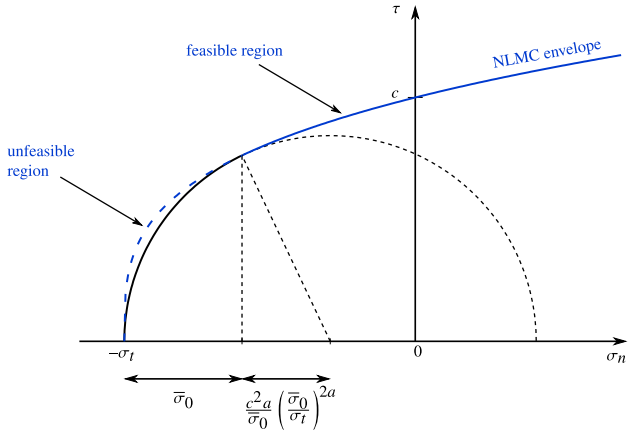

Fig. 3. Non-viable region of the NLMC yield envelope when $a < \frac{1}{2}$.

As shown in Fig. 1, the variable $\overline{\sigma}$ quantifies the horizontal distance between the tangency point, M, and the apex point located at $\sigma_n = -\sigma_t$.

The derivatives can also be calculated using recursive formulas, which are both compact and convenient for computational implementation:

$$\begin{cases} d_0 = c\left(\frac{\overline{\sigma}}{\sigma_t}\right)^a \\ d_{k+1} = d_k \frac{a-k}{\overline{\sigma}} \end{cases} \tag{9}$$

This leads to a simplified expression for the product $d_0 d_1$:

$$d_0 d_1 = \frac{c^2 a}{\sigma_t^{2a}} \overline{\sigma}^{2a-1} \tag{10}$$

To obtain an explicit form of the NLMC criterion in terms of stress invariants, $\overline{\sigma}$ must be eliminated from (4). This is achieved by solving the first equation of (4) for $\overline{\sigma}$. Substituting (10) into (4) transforms the equation into:

$$\frac{c^2 a}{\sigma_t^{2a}} \overline{\sigma}^{2a-1} + \overline{\sigma} - (\sigma_t + \sigma_c) = 0 \tag{11}$$

A closed-form solution for this equation exists only when $a = 1$ or $a = \frac{1}{2}$. In these cases, the equation reduces to a linear form. For all other values of a, the equation must be solved numerically, making it impractical to express the NLMC criterion explicitly in terms of stress invariants. This increases the complexity of the numerical implementation of the criterion.

Before proceeding with the numerical formulation, there is one peculiarity of the NLMC criterion that should be addressed. From (4), the minor principal stress, σ_3, for a plastic stress state is given by:

$$\sigma_3 = \sigma_c - r = -\sigma_t + \overline{\sigma} + d_0 d_1 - d_0 \eta \tag{12}$$

As shown in Fig. 1, the value of σ_3 cannot fall below $-\sigma_t$. An attentive analysis reveals that when solving (12) for the apex point, where $\sigma_3 = -\sigma_t$, another admissible solution can be found in addition to the trivial solution $\overline{\sigma} = 0$, which occurs when $a < \frac{1}{2}$. This effectively dictates a minimum threshold for $\overline{\sigma}$ greater than 0, denoted as $\overline{\sigma}_0$ in the subsequent discussion.

These minimum values, corresponding to different friction angles ($\phi = 10°$, $20°$, $30°$, $40°$, and $50°$), are displayed by the five curves presented in Fig. 2.

The existence of such a threshold implies that certain points on the yield envelope are unattainable, and plasticity occurs when the component σ_3 reaches the yield tensile value $-\sigma_t$. This phenomenon is depicted in Fig. 3. Note that for $a \geq \frac{1}{2}$, the threshold ceases to exist, leading to $\overline{\sigma}_0 = 0$.

Fig. 4 illustrates the NLMC yield envelope in the stress invariants (σ_c, r) space. These invariants represent the average and half-difference

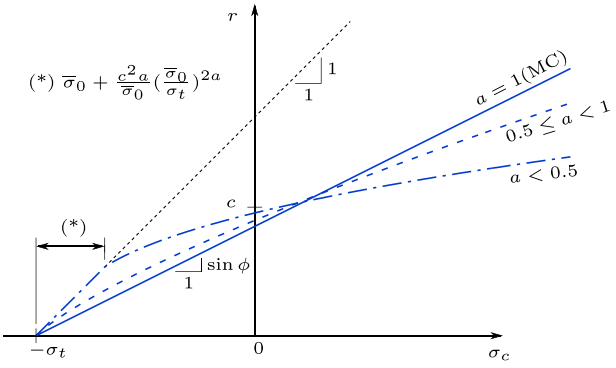

Fig. 4. NLMC yield envelope in the stress invariants (σ_c, r) space.

of the major principal stress σ_1 and the minor principal stress σ_3, respectively:

$$\sigma_c = \frac{\sigma_1 + \sigma_3}{2}, \quad r = \frac{\sigma_1 - \sigma_3}{2} \tag{13}$$

The figure displays three curves, each illustrating the criterion behavior for different values of the nonlinear coefficient a: one for $a = 1$ (representing the classical MC criterion), another for $a < \frac{1}{2}$, and a third one for an intermediate value between 0.5 and 1. We recall that, aside from the MC scenario, it is not feasible to derive an explicit analytical function for these curves. They were obtained resorting to (4).

For the MC criterion ($a = 1$), the yield envelope is a straight line with a slope of $\sin\phi$. For other values of a, the envelope forms a curve with a slope that decreases under higher compressive stress states. When $a < 0.5$, the initial segment of the envelope forms a straight line at a 45° angle. This portion of the curve corresponds to scenarios where plasticity occurs when σ_3 reaches the yield tensile value, a detail discussed earlier.

Additionally, it is noteworthy that the yield envelope curves cross the origin at an ordinate smaller than c, irrespective of the value of the nonlinear coefficient, a.

Determining the slope of the yield envelope curve accurately in the (σ_c, r) space is crucial for the numerical implementation of the NLMC criterion. To accomplish this, we first calculate the derivatives of these invariants with respect to $\overline{\sigma}$. Using the definition provided in (4), we derive the first and second derivatives as follows:

$$\sigma_c' = \frac{d\sigma_c}{d\overline{\sigma}} = 1 + d_0 d_2 + d_1^2 \tag{14}$$

$$\sigma_c'' = \frac{d^2\sigma_c}{d\overline{\sigma}^2} = 3 d_1 d_2 + d_0 d_3 \tag{15}$$

and,

$$r' = \frac{dr}{d\overline{\sigma}} = \frac{d_1}{\eta}\sigma_c' \tag{16}$$

$$r'' = \frac{d^2r}{d\overline{\sigma}^2} = \frac{1}{\eta}\left[d_0\left(d_1d_3 + d_2^2 - \left(\frac{d_1d_2}{\eta}\right)^2\right) + d_2 + 3d_1^2d_2\right] \tag{17}$$

Applying the chain rule in calculus, we have:

$$\frac{dr}{d\sigma_c} = \frac{dr}{d\overline{\sigma}} \cdot \frac{d\overline{\sigma}}{d\sigma_c} = \frac{r'}{\sigma_c'} \tag{18}$$

Thus, by substituting Eqs. (14) and (16) into Eq. (18), we can determine the slope of the yield envelope curve as follows:

$$\frac{dr}{d\sigma_c} = \frac{d_1}{\sqrt{1+d_1^2}} \tag{19}$$

This expression confirms that for $a = 1$, the slope of the yield envelope remains constant. Specifically, in this scenario, $d_1 = \frac{c}{\sigma_t}$ (as per definition (9)), and substituting this value into Eq. (19) yields:

$$\frac{dr}{d\sigma_c} = \frac{c}{\sqrt{\sigma_t^2 + c^2}} = \sin\phi \tag{20}$$

Furthermore, when $a < 1$, the initial slope of the envelope, which is also the maximum possible slope in this context, is given by:

$$\lim_{\overline{\sigma}\to\overline{\sigma}_0} \frac{d_1}{\sqrt{1+d_1^2}} = 1 \tag{21}$$

This conclusion remains valid even when $\overline{\sigma}_0 = 0$, a condition met when $\frac{1}{2} < a < 1$.

As a last note, we determine the coordinates of a point on the curve corresponding to a specified slope, with the value of $1-e$ (where $e \leq 1$). Solving the equation:

$$\frac{d_1}{\sqrt{1+d_1^2}} = 1 - e \tag{22}$$

yields:

$$d_1 = \frac{1-e}{\sqrt{e(2-e)}} \tag{23}$$

And, according to definition (8), we have:

$$d_1 = a\frac{c}{\sigma_t}\left(\frac{\overline{\sigma}}{\sigma_t}\right)^{a-1} \tag{24}$$

Combining Eqs. (23) and (24), we find:

$$\overline{\sigma} = \sigma_t\left(\frac{\sigma_t}{ac}\frac{1-e}{\sqrt{e(2-e)}}\right)^{\frac{1}{a-1}} \tag{25}$$

Finally, this result can be substituted into (4) to obtain the coordinates of σ_c and r.

3. Numerical formulation

The ADMM-based Finite Element Limit Analysis formulation, previously introduced in a collaborative work (Vicente da Silva et al., 2020), serves as the key computational tool in this research. This formulation employs the versatile and robust ADMM optimization algorithm to address the non-linear convex mathematical programming problems intrinsic to computational limit analysis. Detailed derivations and explanations of the upper and lower-bound formulations are provided in the referenced paper. The readers are encouraged to consult our previous publication for a thorough understanding of the ADMM framework and the derivation of the upper and lower-bound finite element formulations. This section solely focuses on the key steps and mathematical underpinnings necessary to incorporate the NLMC criterion into the FELA formulation.

The solution scheme associated with the ADMM method consists of an iterative process. In the context of Finite Element Limit Analysis (FELA), the first step of each iteration involves finding the solution of a linear system of equations, which leads to a velocity field approximation and a respective stress field approximation.

In the case of the lower-bound formulation, these solutions are always statically admissible. This means that the stress approximation satisfies the domain equilibrium equations and stress boundary conditions. However, the velocity approximation is not necessarily compatible, implying that interelement or boundary kinematic conditions may not be satisfied.

In the case of the upper-bound formulation, it is exactly the opposite, the solution is compatible but not necessarily statically admissible.

Up to this point, the solution procedure operates independently of any particular yield criterion, making it universally applicable regardless of yield conditions.

It is only in the subsequent stage that the yield criterion becomes relevant. It is at this point that the lower{upper}-bound formulation begins to enforce the yield{normal flow} rule.

To this end, it is necessary, for every control point, to project the stress state estimate back to the yield surface whenever it lies outside the yield envelope.

Control points refer to points located at the vertices of the finite elements. In this study, we exclusively consider triangular plane strain elements, meaning that each element is associated with 3 control points.

It is important to clarify that the stress state estimate of a control point, also known as the trial stress state, is computed using the stress field approximation obtained from solving the linear system of equations in the first step of the iteration.

Borrowing the terminology from elastoplasticity, we refer to this projection procedure as the return-mapping scheme. In the principal stress space, this projection is orthogonal to the yield surface, corresponding to the closest point on the yield surface to the original trial stress state point.

While closed-form expressions can be derived for conventional yield criteria (such as Tresca, von Mises, Mohr–Coulomb, and Drucker–Prager) to perform the projection, the same is not true for the NLMC criterion. This compels the design of an efficient projection algorithm.

3.1. Return-mapping scheme

The goal of the return-mapping scheme is to project a trial stress that falls outside the yield surface back to the nearest point on the yield envelope.

Let us define a trial stress state by its Mohr's circle invariants, where the center is denoted as σ_c^{tr} and the radius as r^{tr}. Maintaining the notation adopted in Section 2, σ_c and r represent the center and radius of a generic plastic stress state, which is a stress state that lies on the yield surface.

The distance, D, between the trial stress point and a plastic point can be expressed as:

$$D = \sqrt{[(\sigma_c + r) - (\sigma_c^{\text{tr}} + r^{\text{tr}})]^2 + [(\sigma_c - r) - (\sigma_c^{\text{tr}} - r^{\text{tr}})]^2} \tag{26}$$

Simplifying the expression through straightforward algebraic manipulations yields:

$$\frac{D}{\sqrt{2}} = \sqrt{(\sigma_c - \sigma_c^{\text{tr}})^2 + (r - r^{\text{tr}})^2} \tag{27}$$

Comparing Eqs. (26) and (27), we infer that an orthogonal projection into the yield surface in the principal stress space also corresponds to an orthogonal projection into the yield envelope in the (σ_c, r) space. Furthermore, it is observed that the metrics of the two spaces differ by a factor of $\sqrt{2}$, albeit not directly pertinent to our current objectives. More importantly, it should be noted that a similar conclusion cannot be assumed for the (σ_n, τ) space.

In light of the above considerations, the return-mapping procedure is carried out in the (σ_c, r) space. The procedure varies according to the location of the trial stress point. As identified in Fig. 5a, three different scenarios should be considered. For the most straightforward scenario, if the trial point resides in Zone I, the solution, denoted as (σ_c^*, r^*), is provided by the following closed-form expression:

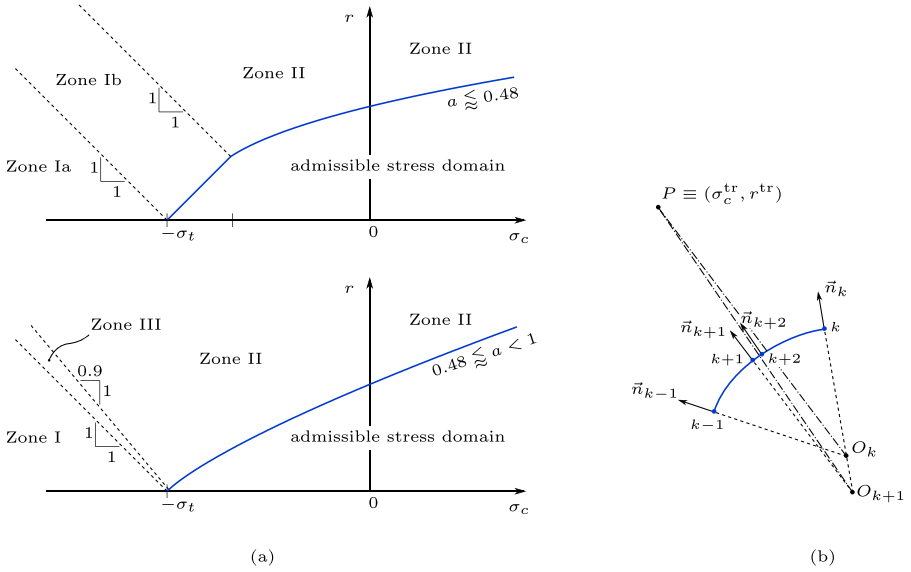

Fig. 5. Return-mapping: (a) projection zones; (b) Zone III algorithm.

$$r^* = \max\left\{0, \frac{\sigma^{tr} + r^{tr} + \sigma_t}{2}\right\} \tag{28}$$

$$\sigma_c^* = r^* - \sigma_t \tag{29}$$

Note that Zone I is subdivided into two regions: Zone Ia encompasses scenarios where the closest point aligns with the yield surface apex ($r^* = 0$), while Zone Ib corresponds to the unfeasible segment of the yield envelope, as depicted in Fig. 2; it exists solely when $a < \frac{1}{2}$.

For points located in Zone II, the closest point projection is determined by finding the stationary point of the distance function (27). Utilizing Eq. (4), the distance function $D(\sigma_c, r)$ is reduced to a single-variable function, $D(\overline{\sigma})$. The stationary condition leads to the following nonlinear equation:

$$\frac{d}{d\overline{\sigma}}\left(\frac{D}{\sqrt{2}}\right) = 0 \Rightarrow g(\overline{\sigma}) = \sigma_c'(\sigma_c - \sigma_0) + r'(r - r_0) = 0 \tag{30}$$

In the absence of a closed-form solution, Newton's method provides an effective alternative for finding the solution numerically. Its iterative formula is given by:

$$\overline{\sigma}_{k+1} = \overline{\sigma}_k - \frac{g(\overline{\sigma}_k)}{g'(\overline{\sigma}_k)} \tag{31}$$

where

$$g'(\overline{\sigma}) = \sigma_c''(\sigma_c - \sigma_0) + (\sigma_c')^2 + r''(r - r_0) + (r')^2, \tag{32}$$

and k represents the iteration number. The definitions of all derivatives involved in the above expressions were derived in Section 2, specifically in Eqs. (14) through (17). Our practical experience reveals that Newton's method, in the present context, demonstrates robust and exceptionally rapid convergence, typically reaching the optimal solution, $\overline{\sigma}_k^*$, in no more than half a dozen iterations, regardless of the initial estimate.

In contrast, within the transition from Zone II to Zone I, known as Zone III, the function $g(\overline{\sigma})$ gradually becomes increasingly ill-conditioned. This renders Newton's algorithm unreliable, exhibiting slow convergence and frequent failure to converge. Therefore, an alternative approach was necessary to address this particular situation. It is worth noting that this phenomenon rapidly diminishes when the value of a drops below 0.5, and around $a = 0.48$, the transitional Zone III ceases to exist, making the alternative algorithm unnecessary.

Fig. 5b demonstrates the method developed for projections located in Zone III. By combining expression (25) with definition (4), any point lying on the yield envelope can be identified by its slope parameter, e. The normal vector to the curve at that point is given by:

$$\vec{n} = -\begin{bmatrix} 1 - e \\ -1 \end{bmatrix} \tag{33}$$

A step of the projection algorithm considers two points on the yield envelope that are close to the optimal solution, identified by the iteration numbers $k-1$ and k. These points are defined by their respective slope parameters, e_{k-1} and e_k.

The circle that best approximates the envelope curve at these two points is centered at the point O_k. The coordinates of the center point can be obtained by solving the following equation:

$$O_k = \begin{bmatrix} \sigma_c(\overline{\sigma}_k) \\ r(\overline{\sigma}_k) \end{bmatrix} + \alpha_k \begin{bmatrix} 1 - e_k \\ -1 \end{bmatrix} = \begin{bmatrix} \sigma_c(\overline{\sigma}_{k-1}) \\ r(\overline{\sigma}_{k-1}) \end{bmatrix} + \beta_k \begin{bmatrix} 1 - e_{k-1} \\ -1 \end{bmatrix} \tag{34}$$

The solution of α_k is,

$$\alpha_k = \frac{\sigma_c(\overline{\sigma}_k) - \sigma_c(\overline{\sigma}_{k-1}) + (1 - e_{k-1})[r(\overline{\sigma}_k) - r(\overline{\sigma}_{k-1})]}{e_k - e_{k-1}} \tag{35}$$

Let $P \equiv (\sigma_c^{tr}, r^{tr})$ be the point defined by the trial stress state. The segment $\overline{PO_k}$ defines the orientation of the normal vector for the next iterate point. Given that $\vec{n}_{k+1} /\!/ \overline{PO_k}$, it is possible to determine the slope parameter for the next iterate point:

$$e_{k+1} = 1 + \frac{\sigma_c(\overline{\sigma}_k) - \sigma_c^{tr} + (1 - e_k)\alpha_k}{r(\overline{\sigma}_k) - r^{tr} - \alpha_k} \tag{36}$$

The iterative process repeats until the slope parameter of two consecutive iterates coincides within a specified tolerance.

The implementation of this algorithm always uses the same starting points: $e_1 = 0.1$ and e_0 is the slope parameter associated with $\overline{\sigma}_0$, determined using Eq. (22). When $\frac{1}{2} \le a < 1$, $e_0 = 0$. If the result from (22) is $e_0 \ge 0.1$, the algorithm is no longer applicable, which corresponds to cases where Zone III is disregarded.

The algorithm always starts with the same initial values: $e_1 = 0.1$ and e_0, the slope parameter associated with $\overline{\sigma}_0$, determined using Eq. (22). When $\frac{1}{2} \le a < 1$, e_0 is set to 0. If (22) results in $e_0 \ge 0.1$, the algorithm becomes inapplicable, indicating that Zone III is disregarded in such cases.

3.2. Plastic admissibility

Prior to applying the return mapping scheme, the FELA formulation requires a check to ensure the trial stress state point meets the yield condition. This involves assessing whether the stress point falls within

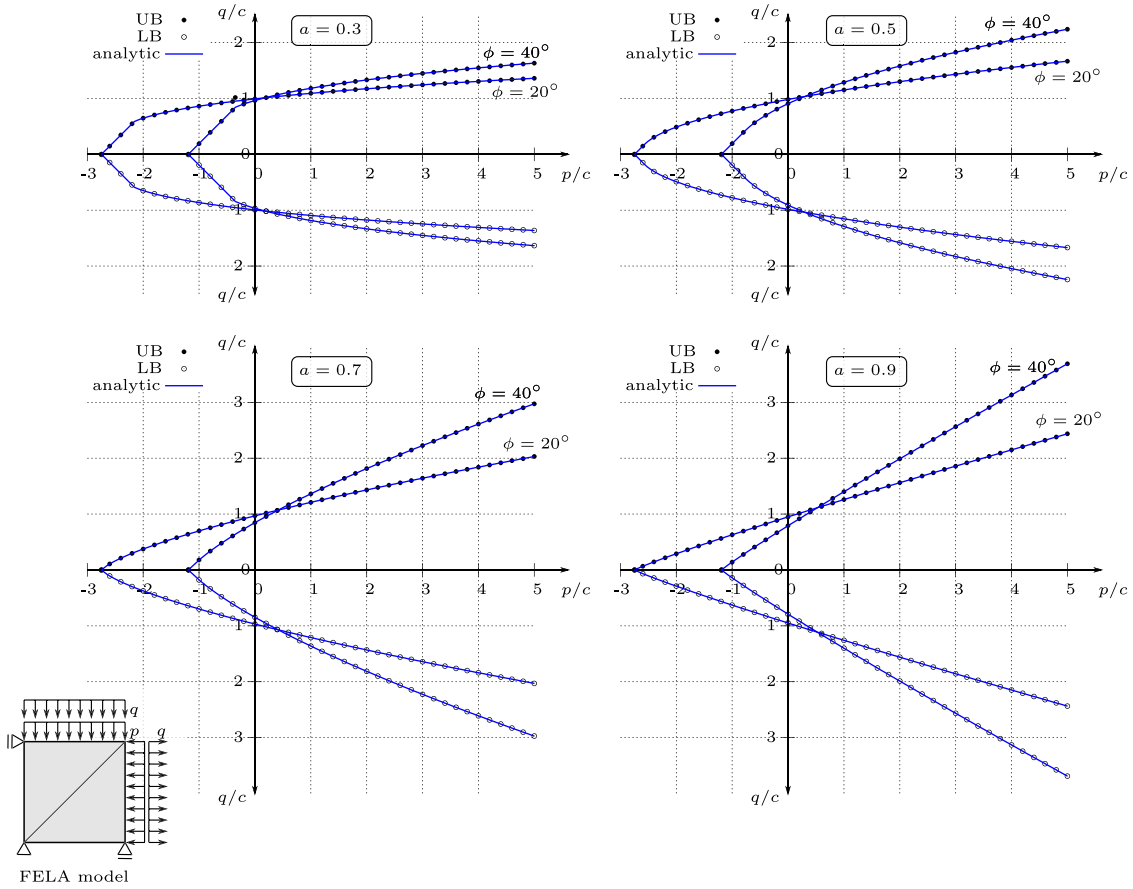

Fig. 6. Validation test based on a biaxial test simulation.

the region enclosed by the yield envelope. If it does, the stress point is considered admissible, and no further action is required.

For many yield conditions, this verification is straightforward. However, in this case, the NLMC criterion complicates the process, as it is not explicitly defined in terms of stress invariants.

An initial approach could be to solve for $\overline{\sigma}$ in the equation:

$$\sigma_c^{\mathrm{tr}} = -\sigma_t + \overline{\sigma} + d_0 d_1 \tag{37}$$

And, subsequently, using this $\overline{\sigma}$, to check if:

$$r^{\mathrm{tr}} \leq d_0 \sqrt{1 + d_1^2} \tag{38}$$

The evident drawback of this approach is that it would require solving (37) numerically, which represents an additional computational cost. Not to mention the potential necessity of dealing with an ill-conditioned problem for some trial points.

The proposed strategy circumvents this issue by directly executing the return-mapping scheme, which halts if, during the iterative process for the kth iterate, it satisfies $\sigma_{c,k} \leq \sigma_c^{\mathrm{tr}}$ and $r_k > r^{\mathrm{tr}}$. This provides sufficient evidence that the trial stress state is plastically admissible.

3.3. Validation

To validate and assess the accuracy and robustness of the numerical implementation of the proposed return-mapping scheme, we conducted simulations of a biaxial test under constant confining pressure, p. Using a two-element model, as shown in Fig. 6, the upper and lower bounds of the shear load, q, were determined for various confinement pressures. The tests considered two different c/σ_T ratios, corresponding to the friction angles of $\phi = 20°$ and $\phi = 40°$. For each friction angle, four different nonlinear coefficients, $a = 0.3$, 0.5, 0.7, and 0.9, were evaluated.

Given the simplicity of the problem, the FELA tool is expected to capture the exact solution, provided that the projection algorithm functions as designed. The study primarily focused on lower confinement levels, as the gradient of the $\tau - \sigma_n$ yield criterion curve changes more abruptly in this region, posing a greater numerical challenge for the return-mapping projection.

Although both the LB and UB formulations rely on the same return-mapping scheme, both were tested independently because, during their respective ADMM iterative processes, they do not necessarily produce identical trial stress states.

As shown in Fig. 6, the numerical tool is definitely capable of accurately reproducing the analytical solution, regardless of the nonlinear parameter value. On the other hand, as discussed in Vicente da Silva et al. (2020), the success of the closest-point projection ensures that the current formulation produces strict collapse load bounds, an important goal of this work.

4. Slope stability analysis

In this section, the classical geotechnical problem of soil slope stability under plane strain conditions is revisited using the newly developed numerical tool. The objective is to study the influence of the nonlinear parameter in the generalized MC strength criterion on the maximum height achievable for an unsupported soil cut with a slope inclination β, considering only the soil's self-weight γ and disregarding any additional surface loading. The soil is assumed to rest on a rigid layer positioned at a depth D. Fig. 7 provides a visual representation of the conditions under investigation. The solution to this problem is quantified by the stability factor, N_s, a dimensionless coefficient defined as:

$$N_s = \frac{\gamma}{c} H^{\max}, \tag{39}$$

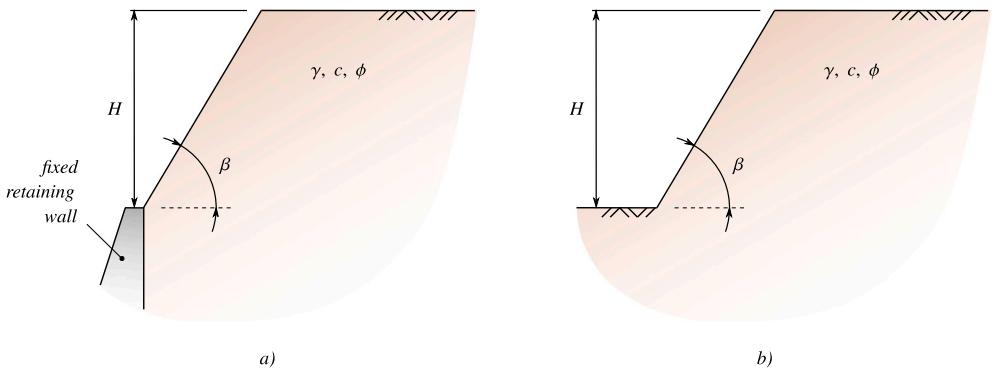

Fig. 7. Definition of the geometry of the slope stability problem: (a) Slope with supported toe, (b) Slope with unsupported toe.

Table 1
N_s stability factors. Part 1 of 4: cases for $a \leq 0.6$ and $\phi \leq 20°$.

ϕ	β	a = 0.3	a = 0.4	a = 0.5	a = 0.6
10°	45°	6.494 ± 0.002	6.781 ± 0.003	7.093 ± 0.003	7.437 ± 0.003
		(6.415 ± 0.003)	(6.742 ± 0.003)	(7.077 ± 0.002)	(7.432 ± 0.003)
	50°	6.195 ± 0.002	6.440 ± 0.003	6.703 ± 0.003	6.990 ± 0.003
		(6.161 ± 0.016)	(6.434 ± 0.003)	(6.701 ± 0.004)	(6.990 ± 0.004)
	60°	5.625 ± 0.002	5.804 ± 0.002	5.996 ± 0.002	6.201 ± 0.002
		(5.623 ± 0.003)	(5.807 ± 0.005)	(5.997 ± 0.003)	(6.201 ± 0.003)
	70°	5.072 ± 0.001	5.204 ± 0.001	5.346 ± 0.002	5.495 ± 0.002
		(5.069 ± 0.005)	(5.206 ± 0.003)	(5.346 ± 0.003)	(5.495 ± 0.003)
	80°	4.524 ± 0.001	4.624 ± 0.003	4.726 ± 0.002	4.834 ± 0.002
		(4.524 ± 0.002)	(4.624 ± 0.004)	(4.726 ± 0.002)	(4.834 ± 0.003)
	90°	3.978 ± 0.004	4.049 ± 0.003	4.122 ± 0.002	4.200 ± 0.001
		(3.976 ± 0.001)	(4.050 ± 0.005)	(4.123 ± 0.002)	(4.201 ± 0.002)
15°	45°	6.826 ± 0.002	7.278 ± 0.007	7.783 ± 0.004	8.369 ± 0.004
		(6.781 ± 0.002)	(7.258 ± 0.002)	(7.780 ± 0.003)	(8.371 ± 0.005)
	50°	6.484 ± 0.002	6.867 ± 0.005	7.290 ± 0.003	7.774 ± 0.004
		(6.478 ± 0.002)	(6.860 ± 0.006)	(7.291 ± 0.004)	(7.774 ± 0.005)
	60°	5.845 ± 0.002	6.126 ± 0.005	6.429 ± 0.003	6.767 ± 0.003
		(5.845 ± 0.002)	(6.124 ± 0.004)	(6.429 ± 0.003)	(6.769 ± 0.004)
	70°	5.239 ± 0.002	5.448 ± 0.005	5.667 ± 0.002	5.908 ± 0.002
		(5.240 ± 0.002)	(5.446 ± 0.004)	(5.668 ± 0.003)	(5.909 ± 0.003)
	80°	4.650 ± 0.001	4.802 ± 0.004	4.962 ± 0.002	5.135 ± 0.002
		(4.650 ± 0.002)	(4.803 ± 0.005)	(4.963 ± 0.003)	(5.136 ± 0.003)
	90°	4.068 ± 0.001	4.180 ± 0.004	4.294 ± 0.002	4.422 ± 0.007
		(4.069 ± 0.001)	(4.180 ± 0.004)	(4.294 ± 0.002)	(4.417 ± 0.002)
20°	45°	7.151 ± 0.002	7.773 ± 0.003	8.514 ± 0.004	9.408 ± 0.005
	50°	6.768 ± 0.002	7.295 ± 0.003	7.911 ± 0.003	8.638 ± 0.004
	60°	6.062 ± 0.002	6.446 ± 0.002	6.883 ± 0.003	7.382 ± 0.003
	70°	5.405 ± 0.001	5.687 ± 0.002	6.001 ± 0.002	6.351 ± 0.003
	75°	5.087 ± 0.001	5.329 ± 0.002	5.595 ± 0.002	5.890 ± 0.002
	80°	4.774 ± 0.002	4.981 ± 0.002	5.207 ± 0.002	5.454 ± 0.002
	90°	4.159 ± 0.002	4.308 ± 0.001	4.468 ± 0.002	4.643 ± 0.003

where c represents the cohesion of the soil.

The strength of the soil is also characterized by the angle ϕ. Based on the definition provided in Eq. (3), ϕ is given by:

$$\phi = \arctan\left(\frac{c}{\sigma_t}\right) \tag{40}$$

For $a = 1$, ϕ represents the conventional friction angle. Although the classical concept of the angle of internal friction is not preserved for other values of a, the angle ϕ will henceforth be loosely referred to as the friction angle.

Two different scenarios were considered: model (a), where the slope is supported at its toe, forcing the failure mechanism to pass through the toe, and model (b), where the toe of the slope is unsupported.

The simulations perform a comprehensive parametric study, considering variations in slope inclination as well as different soil mechanical parameters. Specifically, seven distinct slope angles are analyzed, ranging from $\beta = 45°$ to 90°.

In terms of soil properties, friction angles ϕ are considered, ranging from 15° to 45° in increments of 5°. To determine the influence of the nonlinear coefficient, the parameter a is gradually reduced from 1 (corresponding to the classical MC criterion) to 0.3 in decrements of 0.1 for each friction angle. For $\phi = 20°$, a slope angle of 75° was also included in the analyses to facilitate better comparison with results published by other authors.

Each configuration undergoes two distinct analyses: one to compute a rigorous upper bound of the stability factor and another to establish a rigorous lower bound, bringing the total number of simulations to 1536. The results are summarized in Tables 1 through 4. For a more comprehensive understanding, these results are also presented graphically in Fig. 8, using the average value obtained for the stability factor.

In Tables 1 and 2, the values obtained for slopes with an unsupported toe are shown in parentheses for friction angles of 10° and 15°. The remaining values correspond to the supported toe scenario.

The analyses showed that the support conditions of the slope's toe had a discernible impact on the results only for these lower friction angles, although this impact was not particularly substantial. Specifically, for unsupported toe slopes, failure mechanisms tended to extend slightly beyond the toe, affecting the corresponding stability factors.

Table 2
N_s stability factors. Part 2 of 4: cases for $a > 0.6$ and $\phi \leq 20°$.

ϕ	β	a = 0.7	a = 0.8	a = 0.9	a = 1.0	Other authors a = 1.0 (UB)
10°	45°	7.816 ± 0.003 (7.816 ± 0.005)	8.236 ± 0.004 (8.238 ± 0.006)	8.703 ± 0.004 (8.707 ± 0.009)	9.228 ± 0.005 (9.231 ± 0.008)	+0.084
	50°	7.302 ± 0.003 (7.303 ± 0.005)	7.645 ± 0.004 (7.646 ± 0.005)	8.021 ± 0.004 (8.022 ± 0.006)	8.435 ± 0.005 (8.436 ± 0.006)	+0.135[a]
	60°	6.420 ± 0.003 (6.421 ± 0.003)	6.657 ± 0.003 (6.657 ± 0.004)	6.910 ± 0.003 (6.912 ± 0.005)	7.184 ± 0.003 (7.186 ± 0.006)	+0.045
	70°	5.652 ± 0.002 (5.653 ± 0.003)	5.819 ± 0.002 (5.820 ± 0.003)	5.996 ± 0.003 (5.998 ± 0.004)	6.185 ± 0.003 (6.186 ± 0.004)	+0.015[a]
	80°	4.947 ± 0.002 (4.948 ± 0.003)	5.066 ± 0.002 (5.067 ± 0.003)	5.192 ± 0.002 (5.192 ± 0.003)	5.323 ± 0.002 (5.324 ± 0.003)	−0.003[a]
	90°	4.281 ± 0.002 (4.281 ± 0.002)	4.366 ± 0.005 (4.366 ± 0.003)	4.453 ± 0.002 (4.453 ± 0.002)	4.542 ± 0.005 (4.545 ± 0.002)	+0.023
15°	45°	9.051 ± 0.004 (9.054 ± 0.007)	9.853 ± 0.006 (9.857 ± 0.010)	10.810 ± 0.009 (10.813 ± 0.012)	11.966 ± 0.011 (11.975 ± 0.020)	+0.088
	50°	8.326 ± 0.004 (8.328 ± 0.006)	8.961 ± 0.005 (8.962 ± 0.007)	9.697 ± 0.006 (9.701 ± 0.010)	10.561 ± 0.008 (10.567 ± 0.013)	–
	60°	7.143 ± 0.003 (7.145 ± 0.005)	7.562 ± 0.004 (7.564 ± 0.005)	8.032 ± 0.005 (8.033 ± 0.006)	8.559 ± 0.005 (8.561 ± 0.008)	+0.073
	70°	6.172 ± 0.002 (6.173 ± 0.004)	6.459 ± 0.003 (6.460 ± 0.004)	6.773 ± 0.004 (6.775 ± 0.005)	7.116 ± 0.003 (7.119 ± 0.006)	–
	80°	5.321 ± 0.002 (5.322 ± 0.003)	5.521 ± 0.002 (5.522 ± 0.003)	5.736 ± 0.003 (5.736 ± 0.003)	5.966 ± 0.003 (5.966 ± 0.004)	–
	90°	4.547 ± 0.002 (4.547 ± 0.002)	4.687 ± 0.004 (4.686 ± 0.005)	4.830 ± 0.003 (4.831 ± 0.003)	4.989 ± 0.006 (4.986 ± 0.003)	+0.029
20°	45°	10.507 ± 0.006	11.888 ± 0.009	13.674 ± 0.017	16.060 ± 0.031	+0.020
	50°	9.510 ± 0.005	10.570 ± 0.007	11.883 ± 0.012	13.543 ± 0.019	+0.427[a]
	60°	7.956 ± 0.004	8.625 ± 0.005	9.403 ± 0.006	10.322 ± 0.009	+0.070
	70°	6.744 ± 0.003	7.186 ± 0.003	7.684 ± 0.004	8.244 ± 0.005	+0.096[a]
	75°	6.217 ± 0.003	6.579 ± 0.003	6.982 ± 0.004	7.428 ± 0.005	+0.023
	80°	5.726 ± 0.002	6.024 ± 0.003	6.351 ± 0.003	6.709 ± 0.004	+0.001[a]
	90°	4.825 ± 0.004	5.029 ± 0.003	5.245 ± 0.003	5.458 ± 0.023	+0.047

[a] Data extracted from a chart; accuracy cannot be completely guaranteed.

Table 3
N_s stability factors. Part 3 of 4: cases for $a \leq 0.6$ and $\phi > 20°$.

ϕ	β	a = 0.3	a = 0.4	a = 0.5	a = 0.6
25°	45°	7.476 ± 0.002	8.293 ± 0.003	9.306 ± 0.004	10.590 ± 0.006
	50°	7.052 ± 0.002	7.743 ± 0.003	8.580 ± 0.004	9.614 ± 0.005
	60°	6.281 ± 0.002	6.781 ± 0.002	7.368 ± 0.003	8.063 ± 0.003
	70°	5.572 ± 0.001	5.937 ± 0.002	6.355 ± 0.002	6.836 ± 0.003
	80°	4.899 ± 0.001	5.166 ± 0.002	5.463 ± 0.002	5.797 ± 0.002
	90°	4.251 ± 0.001	4.439 ± 0.003	4.653 ± 0.005	4.879 ± 0.002
30°	45°	7.808 ± 0.002	8.842 ± 0.003	10.181 ± 0.005	11.968 ± 0.008
	50°	7.344 ± 0.002	8.224 ± 0.011	9.316 ± 0.004	10.738 ± 0.006
	60°	6.505 ± 0.002	7.135 ± 0.002	7.898 ± 0.003	8.835 ± 0.004
	70°	5.743 ± 0.002	6.201 ± 0.002	6.739 ± 0.002	7.375 ± 0.003
	80°	5.027 ± 0.001	5.359 ± 0.001	5.738 ± 0.002	6.173 ± 0.002
	90°	4.343 ± 0.001	4.578 ± 0.001	4.841 ± 0.002	5.136 ± 0.002
35°	45°	8.154 ± 0.002	9.437 ± 0.003	11.168 ± 0.006	13.610 ± 0.010
	50°	7.647 ± 0.002	8.728 ± 0.003	10.144 ± 0.004	12.065 ± 0.009
	60°	6.738 ± 0.002	7.516 ± 0.002	8.489 ± 0.003	9.731 ± 0.005
	70°	5.920 ± 0.002	6.483 ± 0.003	7.163 ± 0.003	7.992 ± 0.003
	80°	5.158 ± 0.001	5.564 ± 0.002	6.039 ± 0.002	6.596 ± 0.003
	90	4.436 ± 0.001	4.722 ± 0.001	5.048 ± 0.002	5.418 ± 0.002
40°	45°	8.516 ± 0.002	10.092 ± 0.003	12.308 ± 0.006	15.618 ± 0.011
	50°	7.964 ± 0.002	9.291 ± 0.002	11.097 ± 0.005	13.677 ± 0.008
	60°	6.980 ± 0.002	7.934 ± 0.002	9.164 ± 0.003	10.800 ± 0.005
	70°	6.100 ± 0.001	6.791 ± 0.002	7.643 ± 0.002	8.714 ± 0.004
	80°	5.288 ± 0.002	5.785 ± 0.001	6.374 ± 0.002	7.081 ± 0.003
	90°	4.523 ± 0.001	4.874 ± 0.001	5.274 ± 0.002	5.735 ± 0.002
45°	50°	8.309 ± 0.002	9.924 ± 0.003	12.221 ± 0.007	15.692 ± 0.009
	60°	7.241 ± 0.002	8.402 ± 0.002	9.955 ± 0.004	12.114 ± 0.006
	70°	6.292 ± 0.002	7.132 ± 0.002	8.200 ± 0.003	9.585 ± 0.004
	80°	5.422 ± 0.001	6.026 ± 0.002	6.758 ± 0.002	7.655 ± 0.003
	90°	4.607 ± 0.001	5.033 ± 0.001	5.527 ± 0.003	6.100 ± 0.002

For all other situations, the stability factors are nearly identical, regardless of the toe support conditions, with any discrepancies likely due to differences in the finite mesh discretization. Therefore, we decided not to differentiate them in the presentation of the results.

Moreover, even in cases where the results vary based on the toe support conditions, the differences are minimal and primarily relevant for slope angles below 60°, especially for smaller values of the nonlinear parameter.

Table 4
N_s stability factors. Part 4 of 4: cases for $a > 0.6$ and $\phi > 20°$.

ϕ	β	a = 0.7	a = 0.8	a = 0.9	a = 1.0	Other authors a = 1.0 (UB)
25°	45°	12.268 ± 0.010	14.541 ± 0.014	17.787 ± 0.035	22.779 ± 0.093	–
	50°	10.918 ± 0.007	12.603 ± 0.011	14.857 ± 0.021	18.016 ± 0.061	–
	60°	8.895 ± 0.004	9.903 ± 0.006	11.138 ± 0.011	12.675 ± 0.019	–
	70°	7.389 ± 0.003	8.031 ± 0.004	8.776 ± 0.006	9.645 ± 0.010	–
	80°	6.171 ± 0.002	6.591 ± 0.003	7.061 ± 0.004	7.587 ± 0.006	–
	90°	5.132 ± 0.003	5.407 ± 0.003	5.707 ± 0.003	6.030 ± 0.006	–
30°	45°	14.459 ± 0.014	18.155 ± 0.034	24.101 ± 0.052	35.279 ± 0.154	+0.174
	50°	12.634 ± 0.011	15.269 ± 0.020	19.140 ± 0.047	25.208 ± 0.127	+0.032[a]
	60°	10.005 ± 0.006	11.488 ± 0.009	13.411 ± 0.017	15.516 ± 0.486	+0.399
	70°	8.132 ± 0.004	9.036 ± 0.005	10.124 ± 0.008	11.439 ± 0.019	+0.141[a]
	80°	6.673 ± 0.003	7.245 ± 0.003	7.897 ± 0.006	8.641 ± 0.008	+0.059[a]
	90°	5.465 ± 0.002	5.829 ± 0.003	6.230 ± 0.004	6.667 ± 0.005	+0.012
35°	45°	17.269 ± 0.017	23.299 ± 0.055	34.745 ± 0.090	66.212 ± 1.865	–
	50°	14.793 ± 0.014	18.916 ± 0.035	25.666 ± 0.025	38.933 ± 0.273	–
	60°	11.353 ± 0.008	13.529 ± 0.018	16.536 ± 0.037	20.864 ± 0.071	–
	70°	9.010 ± 0.005	10.270 ± 0.006	11.840 ± 0.013	13.808 ± 0.024	–
	80°	7.250 ± 0.003	8.017 ± 0.005	8.909 ± 0.008	9.941 ± 0.014	–
	90°	5.838 ± 0.003	6.310 ± 0.004	6.833 ± 0.005	7.407 ± 0.010	–
40°	45°	21.010 ± 0.026	31.188 ± 0.207	55.220 ± 0.216	180.558 ± 1.467	+4.22
	50°	17.603 ± 0.017	24.246 ± 0.139	36.867 ± 0.144	70.697 ± 0.448	+22.958[a]
	60°	13.045 ± 0.010	16.254 ± 0.028	21.071 ± 0.071	28.404 ± 0.721	+0.058
	70°	10.077 ± 0.006	11.835 ± 0.013	14.117 ± 0.025	17.146 ± 0.081	−0.286[a]
	80°	7.932 ± 0.004	8.953 ± 0.007	10.163 ± 0.011	11.595 ± 0.031	−0.165[a]
	90°	6.266 ± 0.003	6.869 ± 0.004	7.542 ± 0.007	8.280 ± 0.013	+0.200[a]
45°	50°	21.431 ± 0.040	32.244 ± 0.111	58.542 ± 0.352	201.631 ± 7.566	–
	60°	15.256 ± 0.018	20.087 ± 0.040	28.177 ± 0.135	43.855 ± 0.825	+0.128
	70°	11.421 ± 0.008	13.899 ± 0.021	17.280 ± 0.044	22.043 ± 0.142	–
	80°	8.764 ± 0.005	10.124 ± 0.009	11.775 ± 0.021	13.747 ± 0.037	–
	90°	6.767 ± 0.006	7.535 ± 0.006	8.393 ± 0.009	9.336 ± 0.027	−0.001

[a] Data extracted from a chart; accuracy cannot be completely guaranteed.

And UB estimates of the stability factors, as shown in the tabled values. The last column of Tables 2 and 4 presents the best UB estimates for the stability factor using the classical Mohr–Coulomb (MC) criterion, collected from the works of Kumar (2004) and Kumar and Samui (2006). Some of this data (marked with an asterisk) was extracted from charts, so its accuracy cannot be completely guaranteed. Although the UB estimates obtained by these other authors are based on an alternative approach involving the optimization of semi-analytical collapse mechanisms, there is a very good agreement between both sets of results.

Furthermore, the fact that the present UB estimates are slightly lower than the existing estimates further confirms the accuracy of this study. This comparison also demonstrates that the current approach provides reliable results, at least for the MC criterion.

For the NLMC criterion, solutions for the slope stability problem are less frequently found in the literature. Notably, we reference the works of Zhang and Chen (1987) and Drescher and Christopoulos (1988). Although the study by Zhang and Chen (1987) presents results for a wider range of soil parameters, most of these results are displayed in chart form, making it difficult to guarantee accurate readings. Additionally, the soil parameters adopted in that study fall outside the range considered relevant from an engineering perspective. Consequently, we focus our comparison on the results published by Drescher and Christopoulos (1988). This comparison is illustrated in Fig. 9. The consistency between the two sets of results validates the formulation developed in this paper. Once again, the current UB estimates are slightly lower than the reference values, suggesting a higher quality of results. In fact, in Fig. 9, the difference between the current LB and UB curves is barely noticeable due to the reduced gap between them.

From the analysis of the results, the key conclusion regarding the effect of the nonlinear parameter is that the stability factor decreases significantly as the parameter decreases, and this effect is consistent across all friction angles. Additionally, the reduction of the nonlinear parameter diminishes the differences caused by varying friction angles.

4.1. Computational time analysis

In this subsection, the computational efficiency of the proposed formulation is analyzed, from a computation time perspective, through the evaluation of the computation times required to generate the curves in Fig. 9.

All reported computation times were obtained using a dedicated server equipped with an Intel Xeon E5-2640 hexa-core CPU @ 2.50 GHz, with two threads per core, and 24 GB of memory. The NLMN return-mapping scheme was implemented as a library of *mechpy* (Vicente da Silva and Antão, 2013), an in-house software platform written in Python, intended for the design, implementation, and testing of novel non-conventional finite element formulations. This software was tested on a Linux virtual machine configured with 6 threads and 17 GB of memory.

Another virtual machine with similar characteristics, using the Windows 10 operating system, was employed to execute *OptumG2* (2023 version), a commercial finite element software utilized as a benchmark. *OptumG2* relies on a state-of-the-art limit analysis formulation based on a second-order cone programming (SOCP) solver (Krabbenhoft et al., 2015).

For slopes with $\phi = 20°$, Fig. 10 shows the computational times for the LB analyses, whereas Fig. 11 provides the corresponding details for the UB analysis. In this work, four steps of adaptive remeshing were used to achieve the desired level of accuracy. The reported times pertain to the analyses of the finest meshes obtained in the final remeshing step, which contain approximately 90 000 to 95 000 finite elements.

Figs. 10 and 11 also present the computational times obtained using *OptumG2* software for meshes with a similar number of finite elements. The results are limited to the classical MC criterion, as the software does not support the NLMC criterion. Unfortunately, a comparison with the computational times reported in other FELA studies implementing the NLMC criterion (Li and Cheng, 2012; Korada and Kumar, 2023) is not possible, as the authors did not provide that data.

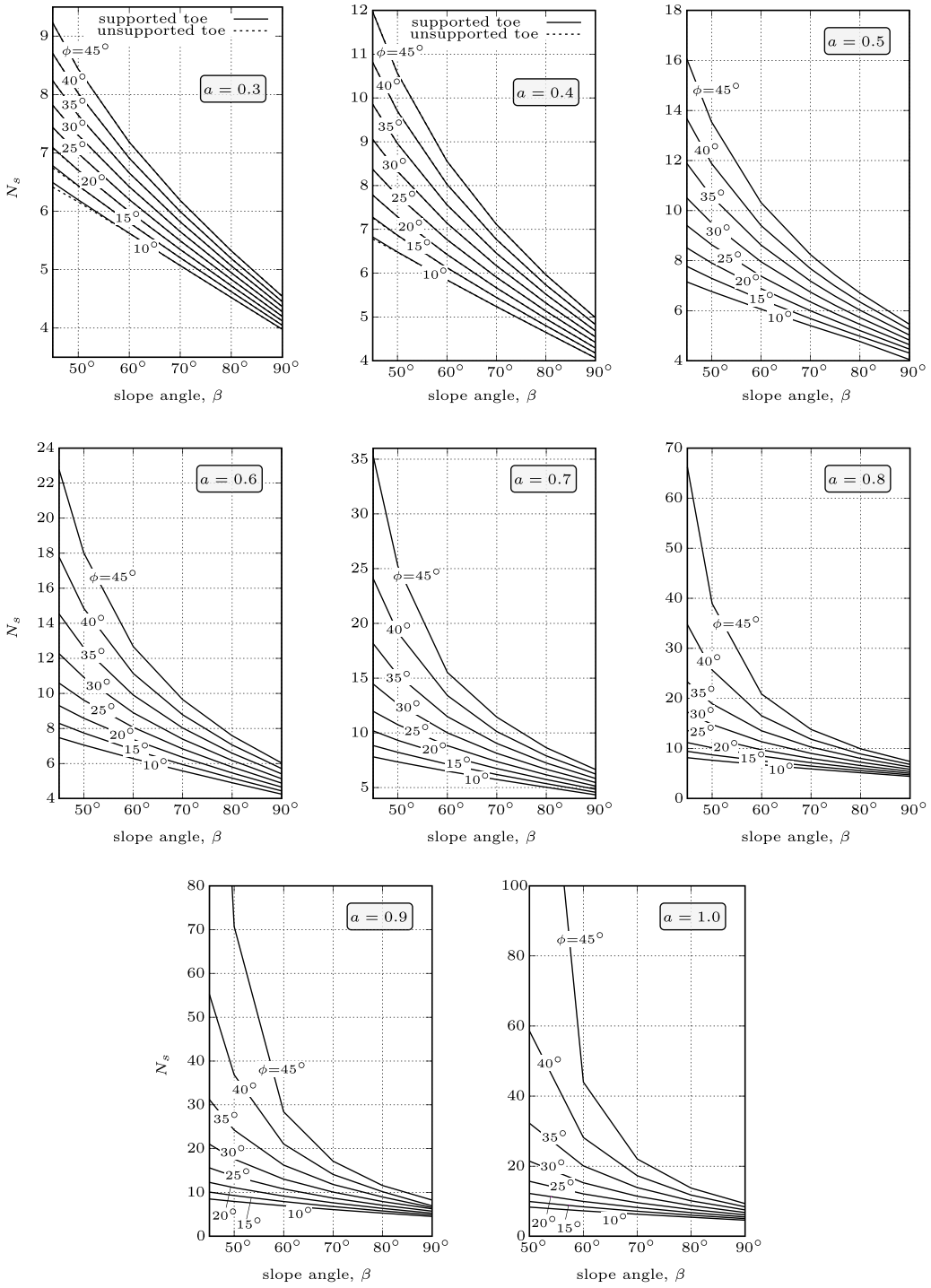

Fig. 8. Impact of nonlinear parameter on average stability factor curves.

The analysis of this data reveals that considering a nonlinear parameter increases the computational effort. In the case of the LB analysis, this represents an increase of around 20%, whereas for the UB analysis, the increase is slightly higher, at approximately 30%. For the UB analysis, it also appears that the increase for cases with $a < 0.5$ tends to be more noticeable than for the other cases; this difference is not observed in the LB examples.

Compared to *OptumG2*, the execution times of the present formulation are, on average, 1.26 and 1.35 times slower for the UB and LB analyses, respectively. This outcome is consistent with the findings of Vicente da Silva et al. (2020), which indicate that the ADMM solver typically becomes competitive with the SOCP approach only in problems involving a significantly larger number of decision variables, a scenario usually encountered in 3D analyses with very fine meshes.

5. Closure

This paper presents the implementation of a nonlinear Mohr–Coulomb criterion within an ADMM-based FELA formulation, with a particular focus on its application to assessing slope stability factors.

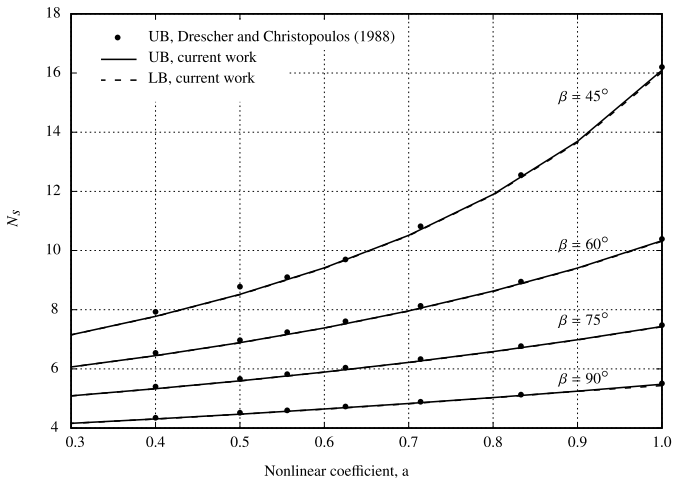

Fig. 9. Comparison of stability factor with varying nonlinear parameter to other authors' proposals for $\phi = 20°$.

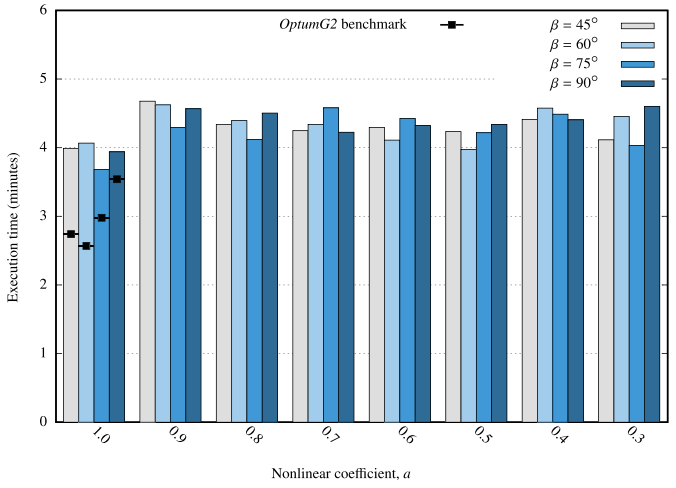

Fig. 10. Execution time evaluation for LB analyses of slopes with $\phi = 20°$.

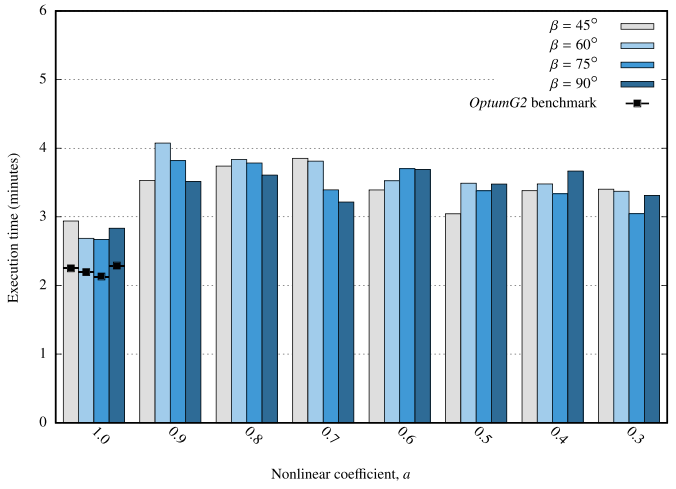

Fig. 11. Execution time evaluation for UB analyses of slopes with $\phi = 20°$.

The return-mapping scheme was developed with strict mathematical rigor, ensuring that the projected stress point precisely lies on the original yield surface. Since the numerical procedure avoids any approximations or smoothing of the yield surface, the solutions produced by this FELA formulation yield rigorous LB and UB estimates.

The numerical results demonstrate the formulation's ability to produce highly accurate results. For the problem at hand, the relative gap between the LB and UB estimates is generally below 0.2%. Larger gaps are observed in analyses involving soils with higher friction angles (above 30°) and a nonlinear parameter of $a \leq 0.8$. Specifically, the maximum gap observed was 3.752% for a slope with $\beta = 50°$, a soil friction angle of $\phi = 45°$, and a nonlinear parameter of $a = 1$. In scenarios involving a nonlinear parameter, the worst-case error was 0.663%, recorded for the analysis with $\beta = 45°$, $\phi = 40°$, and $a = 0.8$.

As a novel contribution, this work presents tables with highly accurate stability factor values for slopes, covering a broad spectrum of soil properties and slope inclinations using the NLMC strength criterion. The findings highlight that the stability factor is notably influenced by the nonlinear parameter, a, with a clear trend of decreasing stability as this parameter decreases. This trend underscores the critical role of soil shear strength under low-confining pressure conditions in slope failure, effectively captured by the proposed approach.

The nonlinear behavior of soils, particularly under low-confinement conditions, is inherently complex. When applying the current predictions to real-world contexts, it is essential to recognize that, while the tool provides near-exact theoretical estimates of stability factors, the limit analysis approach remains a numerical approximation of physical phenomena. Certain simplifications may lead to deviations when comparing the results with field data or experimental findings. Specifically, it assumes perfect plasticity, which precludes the possibility of any hardening or softening, and also assumes plastic flow associativity.

However, this material model offers greater flexibility compared to the classical MC criterion, enabling a better fit to soil strength data obtained from triaxial tests, particularly in low-confinement pressure scenarios. For instance, the commonly adopted practice of introducing a tension cutoff in the MC criterion to address the overestimation of soil strength in tension can be avoided by using the NLMC criterion.

Future research should focus on further validation through case studies of actual slope failures or centrifuge simulations, where comprehensive triaxial test data are available, although such data appear to be scarce and difficult to find in the literature. This will enable more accurate determination of all NLMC constitutive parameters of the soil, enhancing the practical applicability of the current numerical tool.

Declaration of competing interest

The author declares that he has no known competing financial interests or personal relationships that could have appeared to influence the work reported in this paper.

Data availability

No data was used for the research described in the article.

References

Antão, A.N., Vicente da Silva, M., 2022. Three-dimensional limit analysis with Lade-Duncan criterion. Géotech. Lett. 12 (2), 1–7.

Baker, R., Frydman, S., 1983. Upper bound limit analysis of soil with non-linear failure criterion. Soils Found. 23 (4), 34–42.

Bishop, A.W., Webb, D.L., Lewin, P.I., 1965. Undisturbed samples of London clay from the ashford common shaft: Strength-effective stress relationships. Géotechnique 15 (1), 1–31.

Boyd, S., Parikh, N., Chu, E., Peleato, B., Eckstein, J., 2011. Distributed optimization and statistical learning via the alternating direction method of multipliers. Found. Trends Mach. Learn. 3 (1), 1–122.

Chakraborty, T., Salgado, R., 2010. Dilatancy and shear strength of sand at low confining pressures. J. Geotech. Geoenviron. Eng. 136 (3).

Drescher, A., Christopoulos, C., 1988. Limit analysis slope stability with nonlinear yield condition. Int. J. Numer. Anal. Methods Geomech. 12 (3), 341–345. http://dx.doi.org/10.1002/nag.1610120307.

Fukushima, S., Tatsuoka, F., 1984. Strength and deformation characteristics of saturated sand at extremely low pressures. Soils Found. 24 (4), 30–48.

Korada, V.S., Kumar, J., 2023. Finite elements limit analysis formulation using the power type yield criterion for plane strain and axisymmetric stability problems. Comput. Geotech. 162, 105667. http://dx.doi.org/10.1016/j.compgeo.2023.105667.

Krabbenhoft, K., Lyamin, A., Krabbenhoft, J., 2015. Optum computational engineering (OptumG2). Comput. Softw..

Krabbenhøft, K., Lyamin, A., Sloan, S., 2007. Formulation and solution of some plasticity problems as conic programs. Int. J. Solids Struct. 44 (5), 1533–1549.

Krabbenhøft, K., Lyamin, A., Sloan, S., 2008. Three-dimensional Mohr-Coulomb limit analysis using semidefinite programming. Commun. Numer. Methods Eng. 24 (11), 1107–1119.

Kumar, J., 2004. Stability factors for slopes with nonassociated flow rule using energy consideration. Int. J. Geomech. 4 (4), 264–272. http://dx.doi.org/10.1061/(ASCE)1532-3641(2004)4:4(264).

Kumar, J., Rahaman, O., 2020. Lower bound limit analysis using power cone programming for solving stability problems in rock mechanics for generalized Hoek–Brown criterion. Rock Mech. Rock Eng. 53 (7), 3237–3252. http://dx.doi.org/10.1007/s00603-020-02099-y.

Kumar, J., Samui, P., 2006. Stability determination for layered soil slopes using the upper bound limit analysis. Geotech. Geol. Eng. 24 (6), 1803–1819.

Lancelot, L., Shahrour, I., Mahmoud, M.A., 2006. Failure and dilatancy properties of sand at relatively low stresses. J. Eng. Mech. 132 (12), 1396–1399. http://dx.doi.org/10.1061/(ASCE)0733-9399(2006)132:12(1396).

Li, D., Cheng, Y., 2012. Lower bound limit analysis using nonlinear failure criteria. Procedia Earth Planet. Sci. 5, 170–174. http://dx.doi.org/10.1016/j.proeps.2012.01.030, 2012 International Conference on Structural Computation and Geotechnical Mechanics (SCGM 2012).

Makrodimopoulos, A., Martin, C., 2005. Limit analysis using large-scale SOCP optimization. In: 13th Acme Conference: University of Sheffield.

Maksimovic, M., 1989. Nonlinear failure envelope for soils. J. Geotech. Eng. 115 (4), 581–586. http://dx.doi.org/10.1061/(ASCE)0733-9410(1989)115:4(581).

Martin, C., 2005. Exact bearing capacity calculations using the method of characteristics. In: Proc. 11th Int. Conf. of IACMAG Turin.

Nesterov, Y., 2012. Towards non-symmetric conic optimization. Optim. Methods Softw. 27 (4–5), 893–917. http://dx.doi.org/10.1080/10556788.2011.567270.

Pastor, J., Thai, T.-H., Francescato, P., 2003. Interior point optimization and limit analysis: an application. Commun. Numer. Methods Eng. 19 (10), 779–785.

Pastor, F., Thoré, P., Loute, E., Pastor, J., Trillat, M., 2008. Convex optimization and limit analysis: Application to Gurson and porous Drucker-Prager materials. Eng. Fract. Mech. 75, 1367–1382.

Perry, J., 1994. A technique for defining non-linear shear strength envelopes, and their incorporation in a slope stability method of analysis. Q. J. Eng. Geol. 27 (3), 231–241. http://dx.doi.org/10.1144/GSL.QJEGH.1994.027.P3.04.

Ponce, V.M., Bell, J.M., 1971. Shear strength of sand at extremely low pressures. J. Soil Mech. Found. Div. 97 (4), 625–638.

Rahaman, O., Kumar, J., 2020. Stability analysis of twin horse-shoe shaped tunnels in rock mass. Tunn. Undergr. Space Technol. 98, 103354. http://dx.doi.org/10.1016/j.tust.2020.103354.

Smith, C., Gilbert, M., 2007. Application of discontinuity layout optimization to plane plasticity problems. Proc. R. Soc. Lond. Ser. A Math. Phys. Eng. Sci. 463, 2461–2484.

Vicente da Silva, M., Antão, A., 2013. Mechpy's webpage. http://geocluster.dec.fct.unl.pt/mechpy/.

Vicente da Silva, M., Antão, A., 2023. Three-dimensional limit analysis using the Extended-Matsuoka–Nakai yield criterion. Comput. Geotech. 161, 105526.

Vicente da Silva, M., Antão, A., 2024. Computational upper- and lower-bound 3D limit analysis using the hoek-brown yield criterion. Int. J. Geomech. 24 (4), 04024036. http://dx.doi.org/10.1061/IJGNAI.GMENG-9081.

Vicente da Silva, M., Antão, A., 2025. A Finite Element Limit Analysis Formulation using Bishop's Strength Criterion for Anisotropic Undrained Soils. Int. J. Geomech. (accepted for publication).

Vicente da Silva, M., Deusdado, N., Antão, A., 2020. Lower and upper bound limit analysis via the alternating direction method of multipliers. Comput. Geotech. 124, 103571.

Wu, D., Wang, Y., Qiu, Y., Zhang, J., Wan, Y., 2019. Determination of Mohr-Coulomb parameters from nonlinear strength criteria for 3D slopes. Math. Probl. Eng. 2019 (1), 6927654. http://dx.doi.org/10.1155/2019/6927654.

Yang, X.-l., Long, Z.-x., 2015. Roof collapse of shallow tunnels with limit analysis method. J. Cent. South Univ. 22 (5), 1929–1936. http://dx.doi.org/10.1007/s11771-015-2712-6.

Yang, X.-L., Yin, J.-H., 2004. Slope stability analysis with nonlinear failure criterion. J. Eng. Mech. 130 (3), 267–273. http://dx.doi.org/10.1061/(ASCE)0733-9399(2004)130:3(267).

Yu, L., Lyu, C., Wang, M., Xu, T., 2019. Three-dimensional upper bound limit analysis of a deep soil-tunnel subjected to pore pressure based on the nonlinear Mohr-Coulomb criterion. Comput. Geotech. 112, 293–301. http://dx.doi.org/10.1016/j.compgeo.2019.04.025.

Zhang, X.J., Chen, W.F., 1987. Stability analysis of slopes with general nonlinear failure criterion. Int. J. Numer. Anal. Methods Geomech. 11 (1), 33–50. http://dx.doi.org/10.1002/nag.1610110104.

Zhang, R., Smith, C., 2020. Upper-bound limit analysis of soils with a nonlinear failure criterion. Can. Geotech. J. 57 (3), 423–432. http://dx.doi.org/10.1139/cgj-2018-0513.